

## Article

# Design and Experiment of an Autonomous Navigation System for a Cattle Barn Feed-Pushing Robot Based on UWB Positioning

Zejin Chen <sup>1,2</sup>, Haifeng Wang <sup>2</sup>, Mengchuang Zhou <sup>2</sup>, Jun Zhu <sup>2</sup>, Jiahui Chen <sup>2</sup> and Bin Li <sup>1,2,\*</sup> <sup>1</sup> School of Mechanical Engineering, Guangxi University, Nanning 530004, China; zj\_chen@st.gxu.edu.cn<sup>2</sup> Intelligent Equipment Research Center, Beijing Academy of Agriculture and Forestry Sciences, Beijing 100097, China; wanghf@nercita.org.cn (H.W.); zhoumc@nercita.org.cn (M.Z.); zhujun@nercita.org.cn (J.Z.); chenjihui5269@163.com (J.C.)

\* Correspondence: lib@nercita.org.cn

**Abstract:** The autonomous navigation system of feed-pushing robots is one of the key technologies for the intelligent breeding of dairy cows, and its accuracy has a significant influence on the quality of feed-pushing operations. Currently, the navigation methods of feed-pushing robots in the complex environment of cattle barns mainly include visual, LiDAR, and geomagnetic navigation, but there are still problems relating to low navigation accuracy. An autonomous navigation system based on ultra-wideband (UWB) positioning utilizing the dynamic forward-looking distance pure pursuit algorithm is proposed in this paper. First, six anchor nodes were arranged in the corners and central feeding aisle of a 30 × 86 m rectangular standard barn to form a rectangular positioning area. Then, utilizing the 9ITL-650 feed-pushing robot as a platform and integrating UWB wireless positioning technology, a global coordinate system for the cattle barn was established, and the expected path was planned. Finally, the pure pursuit model was improved based on the robot's two-wheel differential kinematics model, and a dynamic forward-looking distance pure pursuit controller based on PID regulation was designed to construct a comprehensive autonomous navigation control system. Subsequently, field experiments were conducted in the cattle barn. The experimental results show that the static positioning accuracy of the UWB system for the feed-pushing robot was less than 16 cm under no-line-of-sight conditions in the cattle barn. At low speeds, the robot was subjected to linear tracking comparative experiments with forward-looking distances of 50, 100, 150, and 200 cm. The minimum upper-line distance of the dynamic forward-looking distance model was 205.43 cm. In the steady-state phase, the average lateral deviation was 3.31 cm, with an average standard deviation of 2.58 cm and the average root mean square error (RMSE) of 4.22 cm. Compared with the fixed forward-looking distance model, the average lateral deviation, the standard deviation, and the RMSE were reduced by 42.83%, 37.07%, and 42.90%, respectively. The autonomous navigation experiments conducted on the feed-pushing robot at travel speeds of 6, 8, and 10 m/min demonstrated that the maximum average lateral deviation was 7.58 cm, the maximum standard deviation was 8.22 cm, and the maximum RMSE was 11.07 cm, meeting the autonomous navigation requirements for feed-pushing operations in complex barn environments. This study provides support for achieving high-precision autonomous navigation control technology in complex environments.

**Keywords:** feed-pushing robot; autonomous navigation system; ultra-wideband; dynamic forward-looking distance; pure pursuit controller



**Citation:** Chen, Z.; Wang, H.; Zhou, M.; Zhu, J.; Chen, J.; Li, B. Design and Experiment of an Autonomous Navigation System for a Cattle Barn Feed-Pushing Robot Based on UWB Positioning. *Agriculture* **2024**, *14*, 694. <https://doi.org/10.3390/agriculture14050694>

Academic Editor: José Lima

Received: 4 April 2024

Revised: 19 April 2024

Accepted: 23 April 2024

Published: 28 April 2024



**Copyright:** © 2024 by the authors. Licensee MDPI, Basel, Switzerland. This article is an open access article distributed under the terms and conditions of the Creative Commons Attribution (CC BY) license (<https://creativecommons.org/licenses/by/4.0/>).

## 1. Introduction

In recent years, the growth of large-scale dairy farming in China has accelerated, becoming the goal of future development. During dairy cow feeding, feed is arched out of the feeding area, which can result in the cows not eating in time, leading to a decrease in the ratio of milk yield to feed consumption. At present, feeding is primarily performed through manual labor, resulting in low operational efficiency and significant manual input,

constituting a major issue [1]. Therefore, the development of a new generation of artificial intelligence technology and unmanned feed-pushing robots is of great significance for improving the economic benefits of pastures [2]. Autonomous navigation systems are a crucial technology for feed-pushing robots. It is difficult to adapt existing navigation technologies, such as geomagnetic navigation, visual navigation, and satellite-positioning navigation, to the complex environments of cattle barns. Therefore, developing an autonomous navigation system tailored to the needs of feed-pushing robots in cattle barns is essential.

At present, the navigation methods of feed-pushing robots encompass geomagnetic navigation, visual navigation, and Lidar navigation. Wan et al. [3] utilized the geomagnetic navigation method with a fuzzy PID control algorithm to achieve magnetic stripe navigation for robots. However, geomagnetic navigation necessitates modifications to a cattle barn, entailing extensive work and restricting a robot's mobility between cowsheds. Navigation methods based on computer vision technology have the advantages of low hardware costs and an abundance of image information. In recent years, scholars have used VSLAM and other technologies to map the environment of cattle barns and locate robots so as to provide environmental and navigation information for robots, which can effectively solve the limitations of geomagnetic navigation [4]. Some scholars have proposed an object recognition model based on multi-task learning and a path extraction method based on machine vision, realizing target recognition and navigation information extraction [5,6]. However, variations in light intensity within cattle barns can significantly impact the performance of visual navigation algorithms [7]. An autonomous navigation system for feed-pushing robots in cattle barns based on laser SLAM can effectively solve the problems of susceptibility to electromagnetic and light intensity changes faced by existing feed-pushing robots [8,9], but the unique structural characteristics of cattle barns make it difficult to obtain accurate navigation information using LiDAR.

Numerous studies have been conducted on autonomous navigation systems in agriculture, including Global Navigation Satellite System (GNSS) [10,11] and visual [12,13], LiDAR [14,15], and multi-sensor fusion navigation systems [16,17]. The fusion of GNSS and inertial measurement unit (IMU) can facilitate high-precision positioning [18,19] and be combined with pure pursuit algorithms to build autonomous navigation systems, which exhibit excellent performance in outdoor environments [20,21]. GNSS are susceptible to signal loss in suppressed environments [22], while visual and LIDAR navigation systems can obtain accurate navigation information under GNSS signal suppression [23]. Zhang et al. [24] and Zhang et al. [25] proposed vision-based and 2D LIDAR-based navigation methods, respectively, for achieving the automatic navigation for agricultural robots. Ultra-wideband (UWB) wireless positioning technology has the characteristics of low power consumption, strong penetration, and accurate positioning [26,27], achieving centimeter-level positioning accuracy in cattle barns [28,29], and it is widely used in the field of agricultural robot navigation. The path-tracking method based on UWB wireless positioning can facilitate accurate positioning and autonomous navigation in outdoor open environments [30–32], but an autonomous navigation system based on UWB positioning for application in cattle barns has not been reported.

In view of this, to address the challenges of instability and limited navigation accuracy in the complex environment of cattle barns, this study proposes a dynamic forward-looking distance pure pursuit algorithm for an autonomous navigation system based on UWB positioning. Initially, UWB positioning technology was employed to establish the global coordinate system of a cattle barn and plan the expected path. Subsequently, the forward-looking distance was redefined, and the pure pursuit model was improved based on two-wheel differential kinematics and a geometric pure pursuit model of feed-pushing robots. Ultimately, a dynamic forward-looking distance pure pursuit controller based on PID adjustment was designed, an autonomous navigation control system was established, and the system's stability and reliability were validated in a cattle barn environment.

## 2. Materials and Methods

### 2.1. Overall Composition of the Test Platform

#### 2.1.1. Hardware Components

In this study, the 9ITL-650 feed-pushing robot (Intelligent Equipment Research Center, Beijing Academy of Agriculture and Forestry Sciences, Beijing, China), integrated with a UWB positioning system, was utilized to construct a test platform for an autonomous navigation system. The structure of the feed-pushing robot's autonomous navigation system is illustrated in Figure 1. The overall structure primarily consists of a robot chassis, a screw-shaped feeding device, and the autonomous navigation system. The 9ITL-650 feed-pushing robot measures 1293 mm in length, 819 mm in width, and approximately 1743 mm in height, with the UWB positioning tag installed at the central point of the drive wheel axis. The motion chassis features a two-wheel differential drive structure, with the servo motor serving as the power component that drives the wheels. The screw conveyor, mounted at the front end of the robot, is primarily used to remix the roughage and concentrate feed in the mixed ration and push it to the dairy cow feeding area.

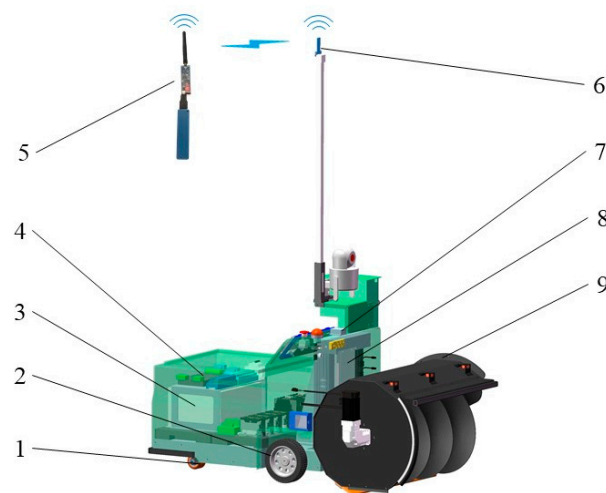


**Figure 1.** Structural diagram of the autonomous navigation system. Note: 1. Universal wheel; 2. Drive wheel assembly; 3. 54 V lithium battery; 4. Microcontroller; 5. UWB positioning system; 6. UWB tag; 7. IMU; 8. Slider; 9. Screw conveyor assembly.

#### 2.1.2. Navigation Control System Architecture

The autonomous navigation system of the feed-pushing robot comprised a UWB positioning system, a control system, and an execution system. The system architecture is illustrated in Figure 2. The UWB positioning system's anchor and tag utilize STM32F103 (STMicroelectronics, Geneva, Switzerland) as the main control chip and DW1000 (DecaWave, Dublin, Ireland) as the ultra-wideband wireless communication chip. The main anchor of the UWB positioning system receives ranging information and calculates tag coordinates. STM32F407 (STMicroelectronics, Geneva, Switzerland) serves as the main control chip of the control system. It receives positioning and IMU attitude data transmitted by the UWB tag via DMA, calculates lateral and heading deviations, and processes these data via the autonomous navigation algorithm to determine the two-wheel motor speed. The motor control command is transmitted to the driver via RS485 communication to realize the autonomous navigation of the feed-pushing robot.

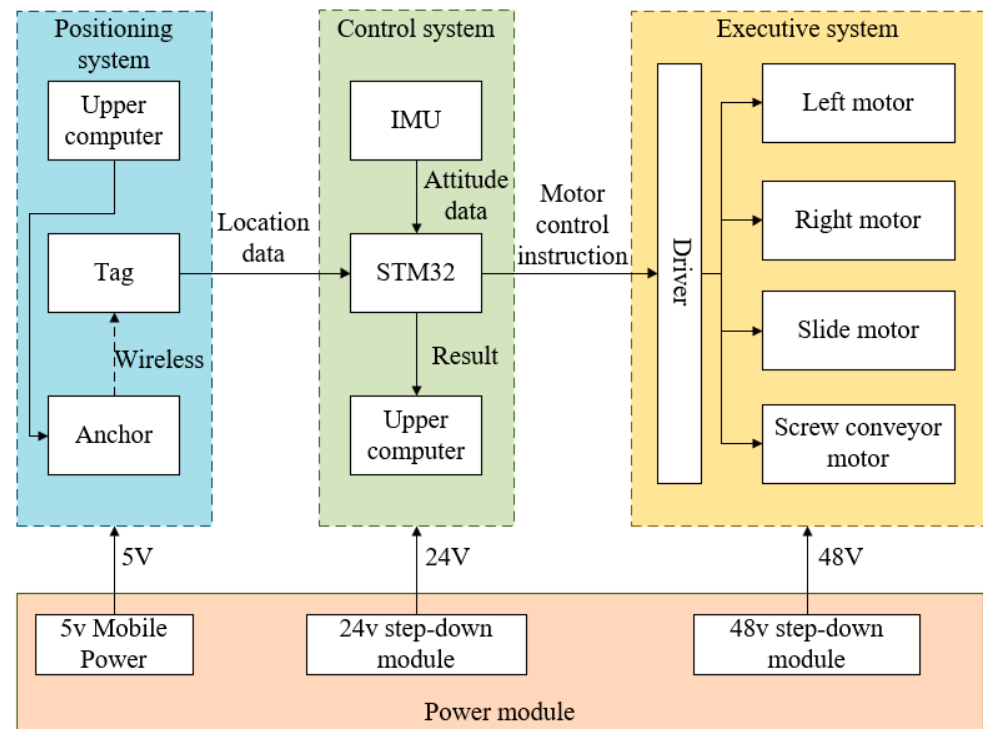


**Figure 2.** Architecture of the autonomous navigation system.

### 2.1.3. Overall Design Method

The control flow of the feed-pushing robot's autonomous navigation system is depicted in Figure 3. The autonomous navigation system comprises positioning, path-planning, and path-tracking components. The UWB positioning system establishes a global coordinate system wherein the starting, end, and turning points are defined. Subsequently, the expected path is planned, and a path-tracking algorithm was developed to actualize the autonomous navigation system. The specific process unfolds as follows:

- (1) Upon powering on, the feed-pushing robot initializes to acquire a real-time position and heading information, with the main controller processing these data at a frequency of 10 Hz.
- (2) Once the screw conveyor descends to its lower limit and begins operation, the dynamic forward-looking distance PID controller calculates the forward distance. Subsequently, the improved pure pursuit algorithm determines the speeds of the left and right wheels, and motor control instructions are transmitted to the driver via RS485 communication to facilitate robot movement.
- (3) When the distance between the robot and the turning point is less than 0.5 m, the turning PID controller takes over to direct the robot's steering.
- (4) The path pursuit algorithm continues to cycle until the distance between the feed-pushing robot's actual position and the final path point is less than 0.5 m, at which point movement and pushing cease.
- (5) Upon completion of this task, the screw conveyor halts operation and ascends to its highest point.

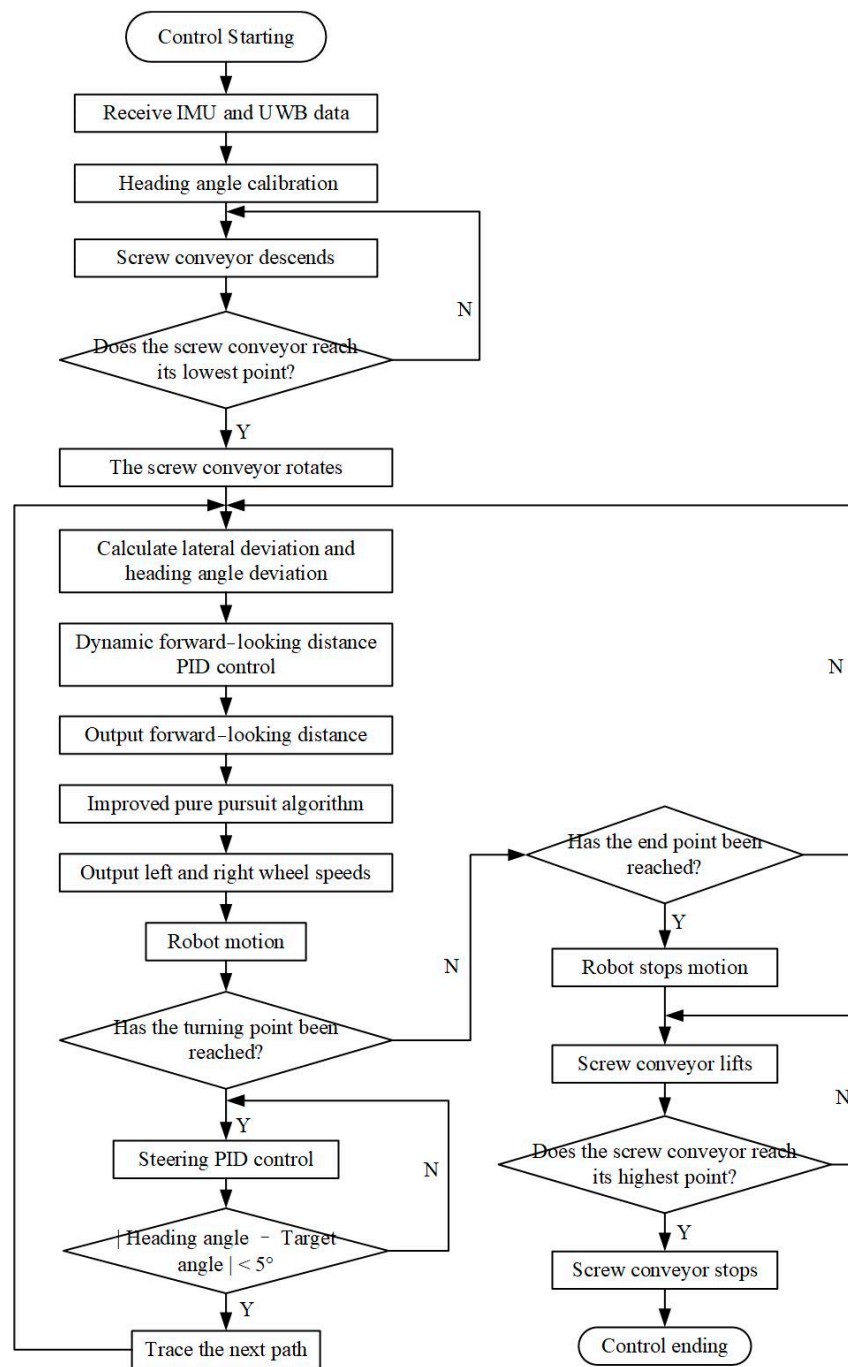
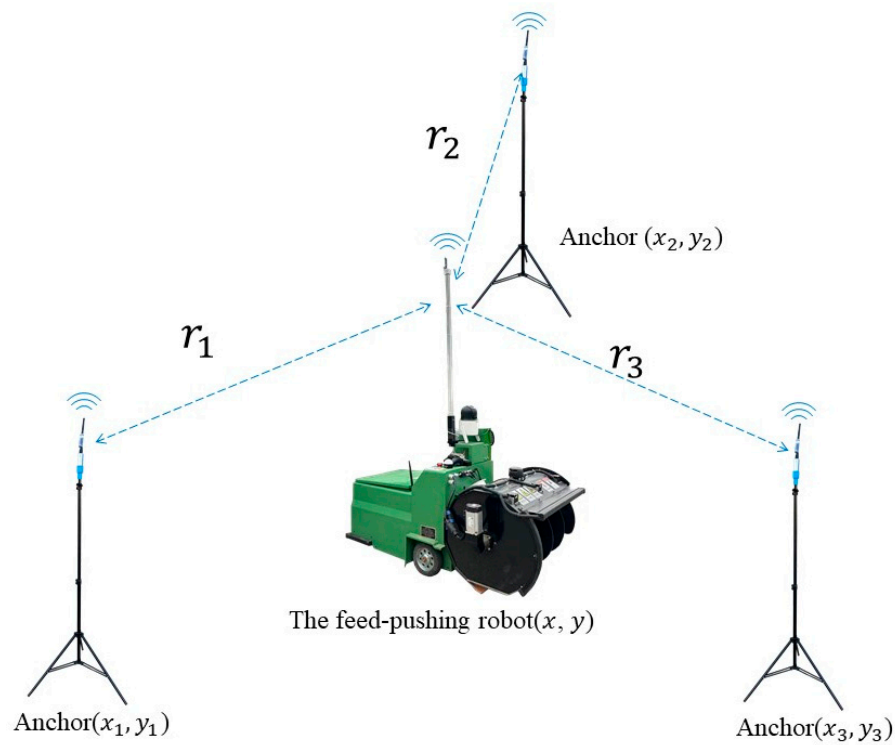


Figure 3. Control flow chart of the autonomous navigation system.

## 2.2. Design of the Autonomous Navigation Controller

### 2.2.1. UWB Location Algorithm

UWB localization is a carrierless communication technique in which a fixed anchor is positioned within the localization area, and the distance between the mobile tag and the fixed anchor is determined by the signal’s time of flight between them. In this research, the distance between the anchor and the tag was calculated using the double-sided two-way ranging (DS-TWR) method. Based on the geometric relationship, the coordinates  $(x, y)$  of the feed-pushing robot could be determined [33,34], as illustrated in Figure 4.



**Figure 4.** The framework of the UWB positioning system.

Based on the DS-TWR positioning principle, the formula for calculating the tag coordinates  $(x, y)$  is as follows:

$$\begin{cases} r_i = c * t_i \\ \sqrt{(x_i - x)^2 + (y_i - y)^2} = r_i \end{cases} \quad (1)$$

where  $r_i$  is the distance from the tag to the anchor in cm;  $c$  is the speed of electromagnetic wave propagation, wherein  $c = 3 \times 10^8$  m/s;  $t_i$  is the signal flight time in s;  $x_i$  is the horizontal coordinate of the anchor in cm;  $y_i$  is the vertical coordinate of the anchor in cm; and  $i$  is the index of the anchor, where  $i = 1, 2, \dots, n$ .

UWB is affected by no-line-of-sight (NLOS) environments, resulting in significant and hard-to-estimate errors in localization results. Consequently, the results of Equation (1) calculations will intersect within a certain area [35]. In this study, the Taylor series algorithm and the least squares method are used to solve the coordinates  $(x, y)$ . The Taylor series expansion can approximate a nonlinear function, and the estimate of the position of the locator tag is corrected iteratively to gradually approximate the true coordinates.

For  $d_i(x, y)$ , Taylor expands at  $(x_0, y_0)$ , neglecting the quadratic terms, as follows:

$$d_i(x, y) = d_i(x_0 + \Delta x, y_0 + \Delta y) + \left. \frac{\partial d_i(x, y)}{\partial x} \right|_{\substack{x = x_0 \\ y = y_0}} \times \Delta x + \left. \frac{\partial d_i(x, y)}{\partial y} \right|_{\substack{x = x_0 \\ y = y_0}} \times \Delta y \quad (2)$$

where  $(x, y)$  are the real coordinates;  $(x_0, y_0)$  are the initial coordinates;  $(x_i, y_i)$  are the  $i$ -th coordinates; the deviation between the real and initial coordinate is  $(\Delta x, \Delta y)$ ; and  $d_i(x, y)$  denote the Euclidean distance between  $(x, y)$  and  $(x_i, y_i)$ .

The matrix equation can be obtained by linearizing Formula (2) as follows:

$$\begin{bmatrix} \Delta x \\ \Delta y \end{bmatrix} = (M^T M)^{-1} M^T N \quad (3)$$

where

$$M = \begin{bmatrix} \frac{x_0-x_1}{\sqrt{(x_0-x_1)^2+(y_0-y_1)^2}} & \frac{y_0-y_1}{\sqrt{(x_0-x_1)^2+(y_0-y_1)^2}} \\ \vdots & \vdots \\ \frac{x_0-x_i}{\sqrt{(x_0-x_i)^2+(y_0-y_i)^2}} & \frac{y_0-y_i}{\sqrt{(x_0-x_i)^2+(y_0-y_i)^2}} \end{bmatrix} \quad N = \begin{bmatrix} d_1 - \sqrt{(x_0-x_1)^2+(y_0-y_1)^2} \\ \vdots \\ d_i - \sqrt{(x_0-x_i)^2+(y_0-y_i)^2} \end{bmatrix}$$

The Kalman filter algorithm can suppress random system noise, and in this study, we adopt the Kalman filter algorithm to suppress noise [36]. Assuming that the position of the coordinates does not change at times  $t$  and  $t - 1$  and there is no external control input, the transfer matrix and the observation matrix constitute the identity matrix. The equations of state and observation are as follows:

$$\begin{cases} \hat{x}_t^- = \hat{x}_{t-1}^- + W_t \\ Z_t = \hat{x}_t^- + V_t \end{cases} \quad (4)$$

where  $\hat{x}_t^-$  is a prior estimate of the state at time  $t$ ;  $Z_t$  is the measurement matrix at time  $t$ ; and  $W_t$  and the  $V_t$  are process and measurement noise, respectively, wherein  $W_t \sim N(0, Q)$  and  $V_t \sim N(0, R)$ .

### 2.2.2. Kinematics Model of the Feed-Pushing Robot

To achieve the autonomous navigation of the feed-pushing robot, designing an autonomous navigation system that meets the precision requirements for the feed-pushing operation is crucial. The feed-pushing robot utilizes the differential speed between two wheels for steering. Assuming that the robot is a rigid body, the model does not account for lateral slip, and tire slippage is considered negligible. The robot's center of mass is located on its longitudinal axis of symmetry. The robot's motion model is shown in Figure 5.

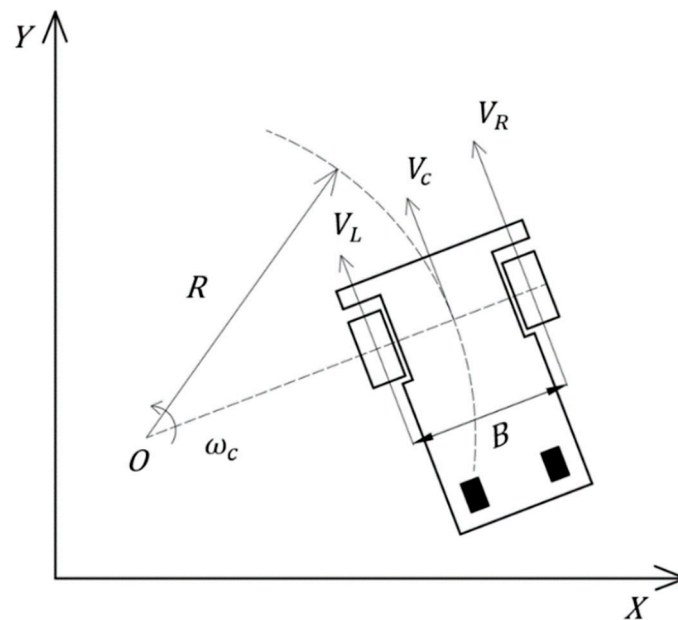


Figure 5. Two-wheel differential motion model.

The relationship for the two-wheel differential kinematics analysis of the feed-pushing robot is as follows:

$$\begin{cases} V_C = \frac{V_R+V_L}{2} \\ R = \frac{B(V_R+V_L)}{2(V_R-V_L)} \\ \omega_C = \frac{V_R-V_L}{B} \end{cases} \quad (5)$$

where  $V_C$  is the movement speed of the feeding-pushing robot in m/s;  $V_L$  and  $V_R$  are the left and right wheel linear speeds in m/s;  $B$  is the two-wheel base of the driving wheel in m;  $R$  is the theoretical turning radius of the pusher robot, with  $O$  as the center, in m; and  $w_C$  is the instantaneous angular velocity of the pusher robot in rad/s.

### 2.2.3. Dynamic Forward-Looking Distance Pure Pursuit Model

The traditional pure pursuit model is a vehicle path-tracking control algorithm based on geometric principles. It calculates the trajectory from a vehicle's current position to the lookahead point by setting a fixed forward-looking distance. However, the traditional pure pursuit model requires the lateral deviation to be less than the forward-looking distance. Therefore, the traditional pure pursuit model is not suitable for operational environments with excessive lateral deviation; hence, the model requires refinement.

The improved pure pursuit model is shown in Figure 6, where  $AB$  represents the expected path and  $P$  denotes the center of the vehicle's front axle. Using the front axle's center point  $P$  as the reference, a perpendicular is drawn from  $P$  to the expected path  $AB$ , with the perpendicular's foot located at  $P'$ . Then, point  $C$  is located along the direction of  $AB$  such that  $P'C = L_d$ , which represents the forward-looking distance. Consequently,  $C$  becomes the lookahead point of the improved pure pursuit model. Based on the geometric relationship, a moving circular arc can be planned, with  $O$  as the center and  $OP$  as the radius.

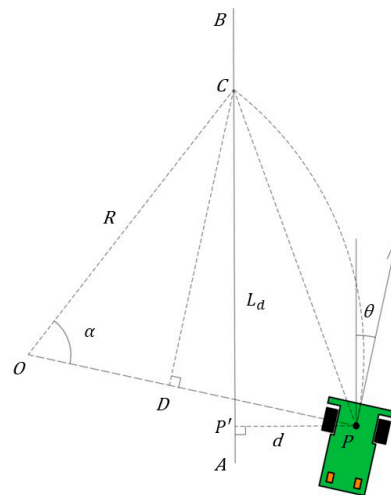


Figure 6. Improved pure pursuit model.

According to the geometric relationship,

$$\begin{cases} L_{PC} = \sqrt{d^2 + L_d^2} \\ L_{DP} = d\cos\theta + L_d\sin\theta \\ \sin\frac{\alpha}{2} = \frac{\sqrt{d^2 + L_d^2}}{2R} \end{cases} \quad (6)$$

where  $L_d$  is the forward-looking distance, given in cm;  $\alpha$  is the central angle corresponding to the robot's moving arc, given in  $^\circ$ ;  $L_{DP}$  is the length of line segment  $DP$ , given in cm;  $d$  is the lateral deviation, given in cm; and  $\theta$  is the heading angle, given in  $^\circ$ .

The formula for calculating the turning radius  $R$  is as follows:

$$R = \frac{d^2 + L_d^2}{2(d\cos\theta + L_d\sin\theta)} \quad (7)$$

The left and right wheel speeds are calculated as follows:

$$\begin{cases} V_R = V_C \left[ 1 + \frac{B(d\cos\theta + L_d \sin\theta)}{d^2 + L_d^2} \right] \\ V_L = V_C \left[ 1 - \frac{B(d\cos\theta + L_d \sin\theta)}{d^2 + L_d^2} \right] \end{cases} \quad (8)$$

According to Equation (8),  $L_d$  represents the only variable parameter and determines the motion radius of the feed-pushing robot. Informed by human driving experience, a larger turning radius is required to expedite the return to the expected path when the deviation is significant. Conversely, a smaller turning radius is necessary to ensure smooth driving when the deviation is minimal. A fixed forward-looking distance results in limited steering adjustability. Given the elongated structures of cattle barns, it is imperative to swiftly rectify deviations during path tracking and reduce oscillations when tracing the desired path. Consequently, this study proposes a dynamic forward-looking distance controller based on PID regulation, which uses the lateral deviation  $d$  as an input and the forward-looking distance as an output to ensure the autonomous navigation system's rapid responsiveness and stability. Figure 7 illustrates the control system structure of the dynamic forward-looking distance PID controller.

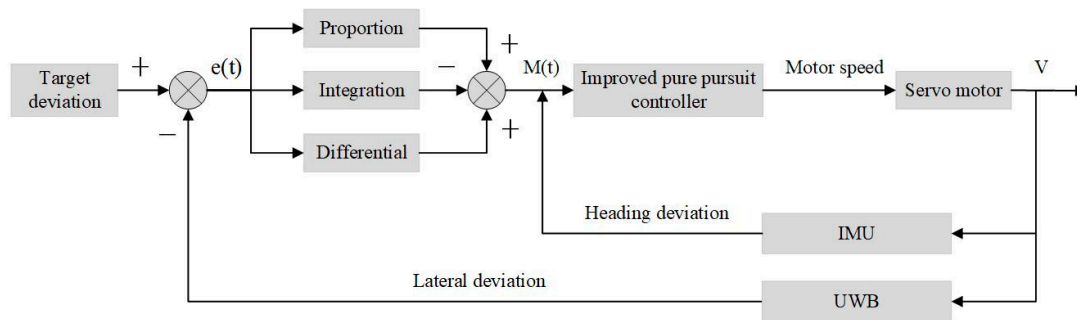


Figure 7. Dynamic forward-looking distance PID controller system structure.

The formula describing the dynamic forward-looking distance discrete PID controller is calculated as follows:

$$M(t) = K_P e(t) + K_I \sum_{t=0}^k e(t) + K_D [e(t) - e(t - 1)] + L_{Init} \quad (9)$$

where  $L_{Init}$  is the initial value of the forward-looking distance, given in cm;  $e(t)$  is the difference between the target deviation and the lateral deviation, given in cm;  $M(t)$  is the dynamic forward-looking distance, given in cm;  $K_P$  is the proportional coefficient;  $K_I$  is the integral coefficient; and  $K_L$  is the differential coefficient.

#### 2.2.4. Design of the Steering PID Controller

In Equation (8), it can be seen that the heading angle deviation was minimal for a straight path, and the improved pure pursuit algorithm demonstrated good passability. However, the continuous expected path featured an abrupt heading angle at the turning point, resulting in an increased turning radius and upper-line distances, causing a significant deviation from the initial state of the next path tracked. To address this issue, a steering controller was designed to adjust the heading angle using in situ steering. The in situ steering controller obtained IMU heading information and calculated the heading deviation in real time, outputting the motor speed through the PID controller to achieve precise steering. When the heading angle was within the threshold range, the feed-pushing robot tracked the next path. The structure of the steering PID controller system is illustrated in Figure 8.

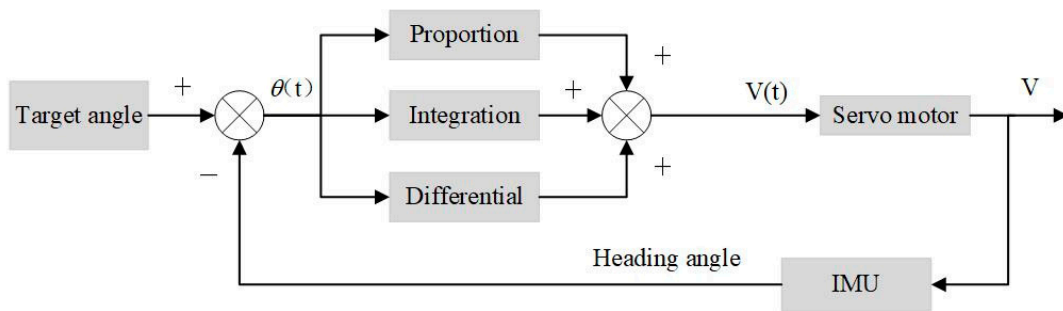


**Figure 8.** Structural diagram of the steering PID controller system.

The steering discrete PID controller achieves control as follows:

$$V(t) = K_p\theta(t) + K_i \sum_{t=0}^k \theta(t) + K_d[\theta(t) - \theta(t-1)] \quad (10)$$

where  $V(t)$  is the wheel speed at time  $t$ , given in m/s;  $\theta(t)$  is the difference between the target heading angle and the heading angle at time  $t$ , given in  $^\circ$ ;  $K_p$  is the proportional coefficient;  $K_i$  is the integral coefficient; and  $K_d$  is the differential coefficient.

### 2.3. System Performance Evaluation Method

To assess the precision and steadiness of the autonomous navigation system, we employed linear-tracking and autonomous navigation performance metrics as evaluative criteria. In these criteria, the stable motion state of linear tracking is defined as the steady state, and the distance required to reach this steady state is referred to as the upper-line distance. The linear tracking performance of the feed-pushing robot was evaluated based on the upper-line distance and steady-state deviation. Lateral deviation, heading deviation, standard deviation ( $\sigma$ ), and the root mean square error (RMSE) were utilized to evaluate the performance of the autonomous navigation system [18]. The vertical distance of the feed-pushing robot to the expected path is termed the lateral deviation, and the angle  $\theta$  between the forward direction and the expected path is termed the heading deviation.

The standard deviation is calculated as follows:

$$\sigma = \sqrt{\frac{1}{Z} \sum_{i=1}^Z (X_i - \bar{X})^2} \quad (11)$$

where  $Z$  is the total number of sampling points;  $X_i$  is the sample value at the  $i$ -th target point, given in cm; and  $\bar{X}$  is the average of the sample values for all target points, given in cm.

The mean square error is calculated as follows:

$$RMSE = \sqrt{\frac{1}{U} \sum_{i=1}^U (Y_i - Y_{ie})^2} \quad (12)$$

where  $U$  is the total number of sampling points;  $Y_i$  is the true value at the  $i$ -th target point, given in cm; and  $Y_{ie}$  is the measured value at the  $i$ -th target point.

## 3. Results and Discussion

This study was conducted from 15 to 16 March 2024, in the adult cow shed at the Treasure Island Ranch owned by Beijing Shounong Animal Husbandry Development Co., Ltd. (Beijing, China) The test site is shown in Figure 9a. The cattle barn alone measured 86 m in length and 30 m in width, and the feeding channel had a width of 5.2 m. In this experiment, we utilized six anchor nodes to establish a rectangular positioning

environment with dimensions of  $60 \times 60$  m, with a uniform installation height of 1.8 m for all nodes. Using the main anchor as the coordinate origin, a Cartesian coordinate system was established, and three expected paths were designed in the feeding channel based on the structural characteristics of the cattle barn and the requirements of the pushing operation. Among these, AB and CD represent the working paths, each 25 m long, while BC is the non-working path, spanning 3 m. The arrows indicate the direction of movement, and point P is any point in the feed-pushing robot's operational trajectory. The actual coordinates of each point were determined using a tape measure. The coordinates of each anchor are as follows:  $(0,0)$ ,  $(2550,0)$ ,  $(6000,0)$ ,  $(0,6000)$ ,  $(2550,6000)$ , and  $(6000,6000)$ . The coordinates of starting point A were  $(2475,1000)$ , and those of end point D were  $(2775,1000)$ . Points B and C were turning points, with coordinates of  $(2475,3500)$  and  $(2775,3500)$ , respectively. The unit of measurement was centimeters, as shown in Figure 9b.

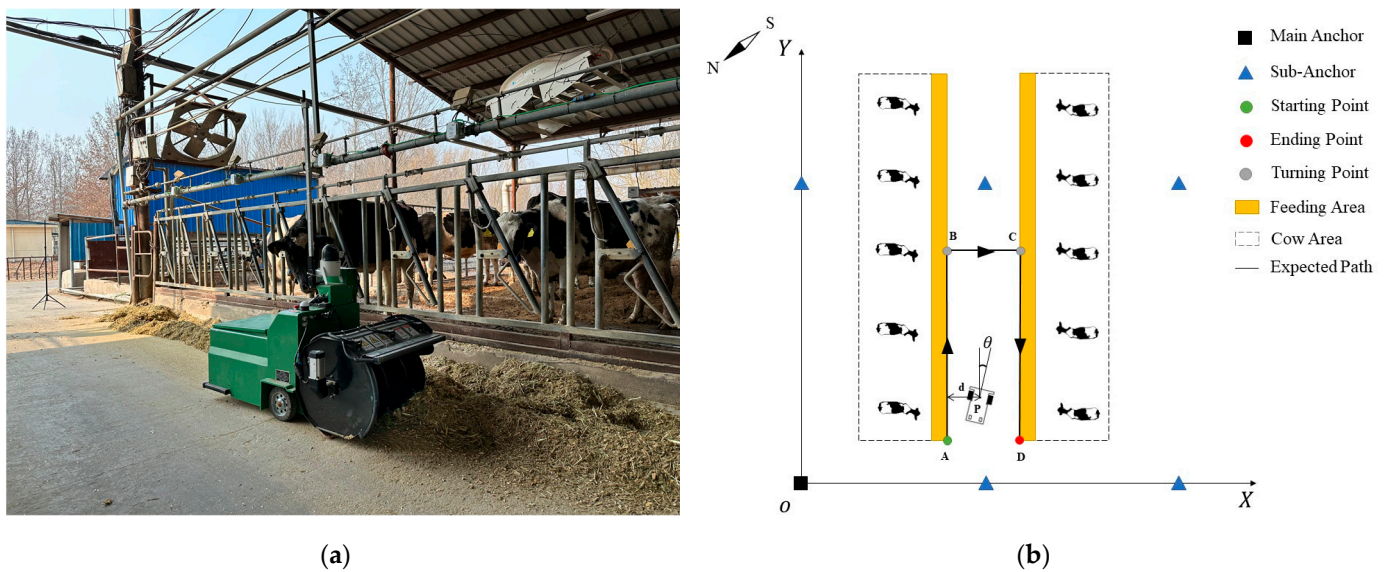


**Figure 9.** Anchor distribution, expected path, and test site diagrams: (a) test site diagram; (b) anchor distribution and expected path diagram.

Each variable was measured three times per group, with the average value serving as the test result. The experiment was divided into three groups:

- (1) A cattle barn UWB positioning system static accuracy test—this test assessed the UWB positioning system's accuracy in the cattle barn's NLOS region.
- (2) A linear tracking test on the cattle barn road—under conditions of consistent deviation and varying initial forward-looking distances, the forward-looking distance and steady-state deviation of the dynamic forward-looking distance model were tested.
- (3) A cattle barn autonomous navigation test—under conditions of an initial state deviation of 0 and varying driving speeds, the feed-pushing robot independently navigated a multi-section path, and its navigation performance, steering performance, and deviation amount were tested.

### 3.1. Static Accuracy Test of the Cattle Barn UWB Positioning System

To assess the effectiveness of the feed-pushing robot's UWB positioning system, a static positioning test was conducted in the cattle barn. Points were selected every 5 m along the planned working path as static positioning test targets, with their true coordinates determined by the perpendicular distances to the x and y axes. The main anchor was connected to the host computer through a micro-USB data cable, with the anchor coordinates  $(x_i, y_i)$  being set. To ensure the system's positioning accuracy, the feed-pushing robot was positioned at the target point with a deviation of  $\pm 5$  cm. When the tag reached the target point, the host computer recorded the coordinates of each target point as experimental

results and calculated the deviation between the target point coordinates and the actual coordinates. The test results are shown in Table 1. The system exhibited a maximum lateral deviation of 16 cm, with average deviations ranging from 6 to 13 cm, standard deviations ranging from 2 to 10 cm, and RMSE values ranging from 7 to 14 cm. The maximum lateral deviation of the pure UWB positioning algorithm in reference [37] was 23.2 cm. Compared with this study, the positioning accuracy after applying Taylor series expansion and the Kalman filtering algorithm was improved by 31.03% compared to the prior reference. The test results show that the static positioning fluctuates within the deviation range. However, the push operation allows a large operating width, and the positioning accuracy met the navigation requirements of feed-pushing robots operating in cattle barns.

**Table 1.** Analysis of the positioning results.

Target Points	Lateral Deviation/cm				Longitudinal Deviation/cm			
	Maximum Values	Mean	Standard Deviation	RMSE	Maximum Values	Mean	Standard Deviation	RMSE
(2475,1000)	14	7.28	6.03	8.45	15	7.56	8.30	8.57
(2475,1500)	15	8.21	8.08	9.18	15	8.28	9.13	9.28
(2475,2000)	14	6.59	4.02	7.72	13	9.14	2.47	9.47
(2475,2500)	15	9.07	4.07	9.94	14	9.67	2.67	10.03
(2475,3000)	15	10.00	4.21	10.85	13	6.47	3.33	7.28
(2475,3500)	14	9.96	4.24	10.82	15	9.6	3.01	10.06
(2775,1000)	15	8.53	3.36	9.17	15	8.84	4.89	10.10
(2775,1500)	15	7.85	4.24	8.92	16	8.38	3.93	9.26
(2775,2000)	15	6.28	4.83	7.92	15	8.00	4.53	9.04
(2775,2500)	13	7.33	3.36	8.06	15	8.89	4.66	10.04
(2775,3000)	16	8.32	3.71	9.11	15	10.28	3.62	10.90
(2775,3500)	15	7.67	4.57	8.93	15	12.93	2.57	13.19

### 3.2. Linear Tracking Test of the Cattle Barn Pavement

The feed-pushing robot was equipped with both a pure pursuit controller with a fixed forward-looking distance and a pure pursuit controller with a dynamic forward-looking distance. The coordinates (2600,1000) and (2600,2500) were chosen as the start and end points, respectively, of the tracking line in the feeding channel, and the robot's starting point coordinates were set to (2700,1000). The driving speed of the feed-pushing robot was set to 8 m/min, and the fixed forward-looking distances were set to 50, 100, 150, and 200 cm, respectively. In the same group test, the initial value  $L_{Init}$  of the dynamic forward-looking distance was set to be the same as that of the fixed forward-looking distance, and the test-driving distance was set to 15 m.

The feed-pushing robot was positioned at the starting point, with an initial lateral deviation of 100 cm (with a deviation of  $\pm 5$  cm) and a heading angle of  $0^\circ$  (with a deviation of  $\pm 2^\circ$ ). The sampling frequency for the test results was set to 5 Hz, and the linear tracking performance was subsequently analyzed. The optimal PID parameters, determined using the test method, were  $PK = 1.5$ ,  $PI = 0.1$ , and  $PD = 0.1$ .

Figure 10 illustrates the horizontal deviation in linear tracking for different forward-looking distances, and the test results are presented in Table 2. The test results indicate that, for the four states, the upper-line distances of the dynamic forward-looking distance model were 205.43, 324.24, 336.15, and 330.42 cm, representing reductions of 32.54%, 27.56%, 28.96%, and 28.87%, respectively, when compared to the fixed forward-looking distance model. The shortest upper-line distance was observed when  $L_{Init} = 50$  cm. As can be seen in Figure 10a,b, the upper-line distance increases significantly when the forward-looking distance is 100 cm. Under the condition that the initial forward-looking distance was 50 cm, the proportional link of the dynamic forward-looking distance PID controller played an obvious role, and the integral and differential links were not enough to compensate for the overshooting of the proportional link, generating a larger curvature in the motion trajectory,

which made the vehicle body approach the expected path quickly, and the upper-line distance obviously shortened. From Figure 10b–d, it can be seen that for the dynamic forward-looking distance model, following the increase in the initial forward-looking distance of the upper-line distance, which changed slowly, the dynamic forward-looking distance PID controller’s integral and differential links compensated for the overshoot of the proportional link. The generated curvature of the motion trajectory thus became smaller, allowing the vehicle body to slowly approach the expected path, and the change in the upper-line distance decelerated.

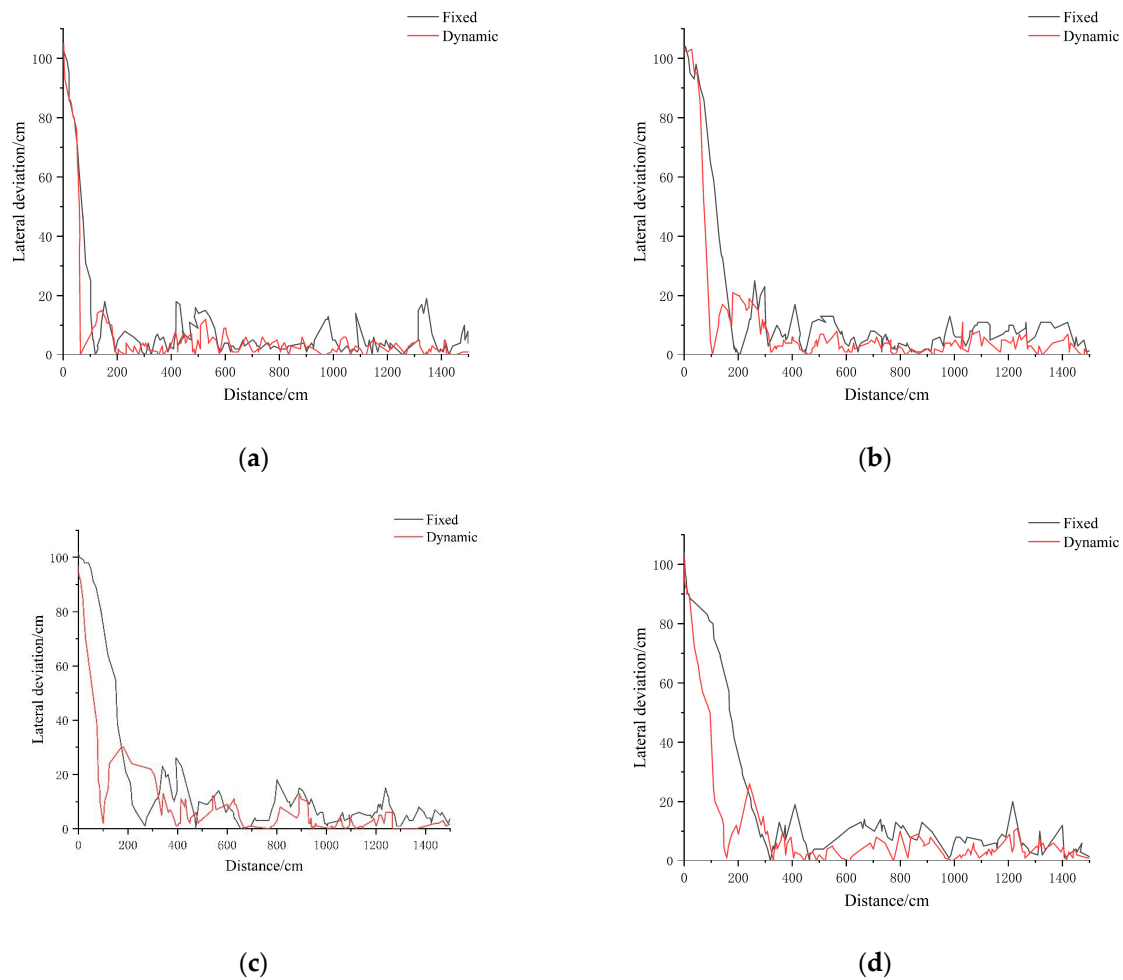


**Figure 10.** Linear tracking lateral deviation at different forward-looking distances: (a) 50 cm; (b) 100 cm; (c) 150 cm; (d) 200 cm.

**Table 2.** Comparison of the linear tracking results.

Tracking Model	Forward-Looking Distance/cm	The Upper-Line Distance/cm	Maximum Lateral Deviation/cm	Mean Lateral Deviation/cm	Standard Deviation/cm	RMSE/cm
Fixed	50	304.52	19.21	5.03	4.40	6.68
	100	447.61	13.58	5.12	3.62	7.19
	150	473.16	18.73	6.26	4.32	7.83
	200	464.55	20.67	6.75	4.06	7.87
Dynamic	50	205.43	12.13	3.05	2.15	3.74
	100	324.24	11.47	3.09	2.05	3.71
	150	336.15	12.51	3.25	3.47	4.75
	200	330.42	11.31	3.85	2.63	4.66

In the steady-state phase, the mean lateral deviations of the dynamic forward-looking distance model were 3.05, 3.09, 3.25, and 3.85 cm, resulting in a mean value of 3.31 cm, a mean standard deviation of 2.58 cm, and a mean RMSE of 4.22 cm. For the fixed forward-looking distance model, the mean lateral deviations were 5.03, 5.12, 6.26, and 6.75 cm, resulting in a mean value of 5.79 cm, a mean standard deviation of 4.10 cm, and a mean RMSE of 7.39 cm. Compared to the fixed forward-looking distance model, the average lateral deviation of the dynamic model was reduced by 42.83%, the standard deviation was reduced by 37.07%, and the RMSE was reduced by 42.90%. The test results reveal that the lateral deviation decreases as the vehicle body approaches the expected path. Consequently, the proportional link of the dynamic forward-looking distance PID controller weakens, leading to a larger output forward-looking distance and a smaller curvature of the generated motion trajectory. This leads to the smoother movement of the vehicle body, with the average lateral deviation remaining below 4 cm across all four forward-looking distance statuses. This result indicates that the dynamic forward-looking distance model exhibited less dispersion in average deviation and a superior online response efficiency and linear tracking performance compared to the fixed model. In comparison to this study, reference [32] proposed an improved pure tracking model path-tracking algorithm with a steady state deviation of 5.9 cm and a maximum lateral deviation of 78.9 cm, resulting in an increase in steady-state deviation accuracy and maximum lateral deviation accuracy by 28.47% and 84.63%, respectively. Reference [38] proposed an autonomous navigation system based on ultra-wideband, achieving a maximum deviation of 18 cm for path tracking and an increase in maximum lateral deviation accuracy by 3.05%. In summary, the dynamic forward-looking distance pure pursuit navigation controller can achieve a steady state faster and enhance the straightness of the pushing operation with robust performance on the same path.

### 3.3. Cattle Barn Autonomous Navigation Test

To evaluate the performance stability of the feed-pushing robot's autonomous navigation system, tests were conducted at various driving speeds. Typically, the operating speed of the feed-pushing robot was 8 m/min, with driving speeds set to 6, 8, and 10 m/min, respectively. The geometric center of the feed-pushing robot's body was 1.1 m from the cowshed barrier, with the screw conveyor's fixed speed set to 37.5 r/min. The test began at starting point A and stopped at end point D. The initial lateral deviation was  $\pm 5$  cm, and the initial heading angle deviation was  $\pm 2^\circ$ . The test results were sampled at a frequency of 5 Hz. When the feed-pushing robot was less than 0.5 m from the turning point, it rotated  $90^\circ$  in place and began tracking the next path. When the robot was less than 0.5 m from the end point, it ceased movement. Table 3 presents the navigation results for different speeds.

**Table 3.** Navigation tracking results at different speeds.

Speed/m/min	Maximum Lateral Deviation/cm	Mean Lateral Deviation/cm	Standard Deviation/cm	RMSE/cm	Mean Heading Deviation/ $^\circ$
6	25.33	7.58	6.86	10.23	4.46
8	32.64	7.10	5.77	9.15	2.53
10	33.29	7.41	8.22	11.07	2.82

The test results indicate that the maximum lateral deviations of the feed-pushing robot were 25.33, 32.64, and 33.29 cm at driving speeds of 6, 8, and 10 m/min, respectively. The maximum lateral deviation of the robot's body occurred at the turning point because the lateral deviation was not zero when tracking the next expected path. The robot's body continuously corrected the deviation and accelerated convergence with the expected path. At the three driving speeds, the average lateral deviations were 7.58, 7.10, and 7.41 cm; the standard deviations were 6.86, 5.77, and 8.22; and the RMSEs were 10.23, 9.15, and 11.07 cm, respectively. The fluctuation range of the average lateral deviation was less than

0.5 cm. The fluctuation ranges of the standard deviation and RMSE were less than 2.5 cm, and the average heading angle error was less than  $5^\circ$ . These results indicate that there was no significant turning or lateral deviation during autonomous navigation, indicating stable navigation performance. The actual trajectory of the autonomous navigation operation depicted in Figure 11 indicates that the deviation during operational paths is significantly larger compared to that during non-operational paths. This is primarily due to the uneven distribution of feed during the pushing operation, resulting in varying resistance between the left and right wheels, and ultimately causing lateral deviation of the vehicle body. In comparison to this study, reference [20] proposed using linear interpolation to acquire path-tracking points, without considering scenarios involving significant lateral deviation. Ref. [25] proposed a 2D LiDAR-based navigation algorithm, achieving an average lateral deviation of 8 cm and enhancing accuracy by 5.25%. Ref. [31] proposed a fuzzy control algorithm, featuring an average error of 18.5 cm and a remarkable accuracy improvement of 59.03%. In summary, the feed-pushing robot can navigate autonomously at various speeds, execute steady turns, and move smoothly in a straight line. The autonomous navigation system can meet the requirements of pusher operation in cattle barns.

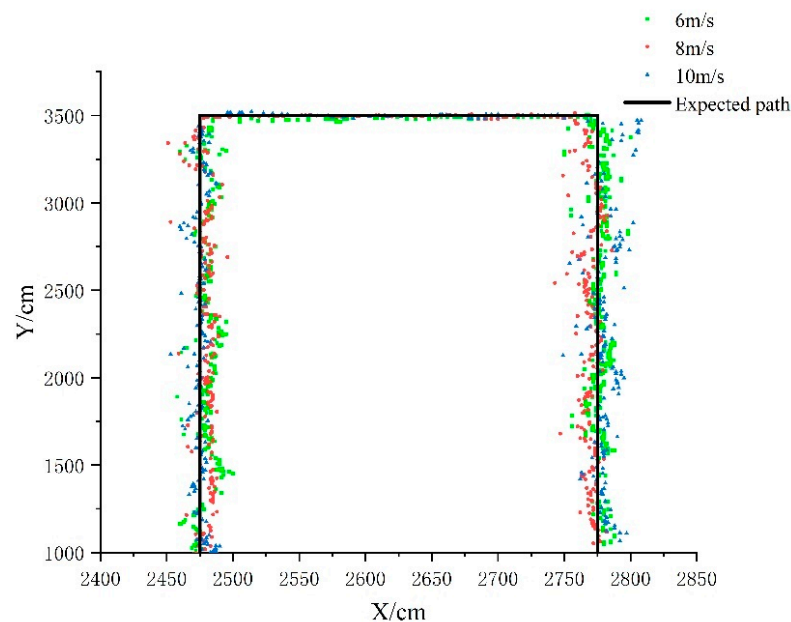


**Figure 11.** The actual trajectory of the autonomous navigation operation.

#### 4. Conclusions

In this study, we designed an autonomous navigation system for feed-pushing robots operating in cattle barns based on UWB positioning, enabling the positioning and autonomous navigation of robots in an NLOS environment. The dynamic forward-looking distance pure pursuit model, compared to the fixed forward-looking distance model, reduced the linear tracking upper-line distances by 32.54%, 27.56%, 16.45%, and 28.87%, respectively. In the steady-state phase, the average lateral deviation, standard deviation, and RMSE decreased by 42.83%, 37.07%, and 42.90%, respectively. The maximum lateral deviation in the feed-pushing robot's autonomous navigation was less than 33.29 cm, the average lateral deviation was less than 7.58 cm, the standard deviation was less than 8.22 cm, the RMSE was less than 11.07 cm, and the average heading angle error was less than  $5^\circ$ . These results demonstrate that the navigation system can operate stably in a cattle barn environment, exhibiting a good navigation performance. Importantly, this method addresses the challenges of autonomous navigation failure in feed-pushing robots due to the absence of GNSS signals in indoor environments, interference with depth cameras caused by environmental information, and difficulties in obtaining navigation data from

LiDAR, providing a reliable research approach for the stable navigation of feed-pushing robots in cattle barns.

**Author Contributions:** Conceptualization, Z.C. and B.L.; Methodology, Writing—original draft, Z.C.; Writing—review editing, H.W., M.Z., J.Z., J.C. and B.L. All authors have read and agreed to the published version of the manuscript.

**Funding:** This work was supported by the National Key Research and Development Program of China (2022YFD1301103).

**Institutional Review Board Statement:** Not applicable.

**Data Availability Statement:** No new data were created or analyzed in this study. Data sharing is not applicable to this article.

**Conflicts of Interest:** The authors declare no conflicts of interest.

## References

1. Methu, J.; Owen, E.; Abate, A.; Tanner, J.C. Botanical and nutritional composition of maize stover, intakes and feed selection by dairy cattle. *Livest. Prod. Sci.* **2001**, *71*, 87–96. [[CrossRef](#)]
2. Rumba, R.; Nikitenko, A. Development of free-flowing pile pushing algorithm for autonomous mobile feed-pushing robots in cattle farms. In Proceedings of the 17th International Scientific Conference Engineering for Rural Development, Latvia, Jelgava, 23–25 May 2018. [[CrossRef](#)]
3. Wan, C.; Tan, Y.; Zheng, Y.; Wen, W.; Yang, S.; Li, B. Automatic Charging of Forage Pushing Robot by Magnetic Stripe Navigation. *Trans. Chin. Soc. Agric. Mach.* **2018**, *49*, 1–7+41. [[CrossRef](#)]
4. Schörghuber, M.; Wallner, M.; Jung, R.; Humenberger, M.; Gelautz, M. Vision-based Autonomous Feeding Robot. In Proceedings of the OAGM Workshop 2018 Medical Image Analysis, Hall/Tirol, Austria, 15–16 May 2018; pp. 111–115. [[CrossRef](#)]
5. Tian, F.; Hu, G.; Yu, S.; Wang, R.; Song, Z.; Yan, Y.; Huang, H.; Wang, Q.; Wang, Z.; Yu, Z. An efficient multi-task convolutional neural network for dairy farm object detection and segmentation. *Comput. Electron. Agric.* **2023**, *211*, 108000. [[CrossRef](#)]
6. Tian, F.; Hu, G.; Yu, S.; Wang, R.; Song, Z.; Yan, Y.; Li, F.; Wang, Z.; Yu, Z. Navigation Path Extraction and Experimental Research of Pusher Robot Based on Binocular Vision. *Appl. Sci.* **2022**, *12*, 6641. [[CrossRef](#)]
7. Wang, T.; Chen, B.; Zhang, Z.; Li, H.; Zhang, M. Applications of machine vision in agricultural robot navigation: A review. *Comput. Electron. Agric.* **2022**, *198*, 107085. [[CrossRef](#)]
8. Tian, F.; Wang, X.; Yu, S.; Wang, R.; Song, Z.; Yan, Y.; Li, F.; Wang, Z.; Yu, Z. Research on Navigation Path Extraction and Obstacle Avoidance Strategy for Pusher Robot in Dairy Farm. *Agriculture* **2022**, *12*, 1008. [[CrossRef](#)]
9. Song, H.; Duan, Y.; Li, R.; Jiao, Y.; Wang, Z. Autonomous Navigation System for Pasture Intelligent Overthrowing Grass Robot Based on Laser SLAM. *Trans. Chin. Soc. Agric. Mach.* **2023**, *54*, 293–301. [[CrossRef](#)]
10. Jing, Y.; Li, Q.; Ye, W.; Liu, G. Development of a GNSS/INS-based automatic navigation land levelling system. *Comput. Electron. Agric.* **2023**, *213*, 108187. [[CrossRef](#)]
11. Huang, Y.; Fu, J.; Xu, S.; Han, T.; Liu, Y. Research on Integrated Navigation System of Agricultural Machinery Based on RTK-BDS/INS. *Agriculture* **2022**, *12*, 1169. [[CrossRef](#)]
12. Opiyo, S.; Okinda, C.; Zhou, J.; Mwangi, E.; Makange, N. Medial axis-based machine-vision system for orchard robot navigation. *Comput. Electron. Agric.* **2021**, *185*, 106153. [[CrossRef](#)]
13. Ma, Y.; Zhang, W.; Qureshi, W.S.; Gao, C.; Zhang, C.; Li, W. Autonomous navigation for a wolfberry picking robot using visual cues and fuzzy control. *Inf. Process. Agric.* **2021**, *8*, 15–26. [[CrossRef](#)]
14. Jones, M.H.; Bell, J.; Dredge, D.; Seabright, M.; Scarfe, A.; Duke, M.; MacDonald, B. Design and testing of a heavy-duty platform for autonomous navigation in kiwifruit orchards. *Biosyst. Eng.* **2019**, *187*, 129–146. [[CrossRef](#)]
15. Liu, L.; Liu, Y.; He, X.; Liu, W. Precision Variable-Rate Spraying Robot by Using Single 3D LIDAR in Orchards. *Agronomy* **2022**, *12*, 2509. [[CrossRef](#)]
16. Xie, B.; Jin, Y.; Faheem, M.; Gao, W.; Liu, J.; Jiang, H.; Cai, L.; Li, Y. Research progress of autonomous navigation technology for multi-agricultural scenes. *Comput. Electron. Agric.* **2023**, *211*, 107963. [[CrossRef](#)]
17. Liu, P.; Bi, S.; Zang, G.; Wang, W.; Gao, Y.; Deng, Z. Obstacle avoidance system for agricultural robots based on multi-sensor information fusion. In Proceedings of the 2011 International Conference on Computer Science and Network Technology (ICCSNT), Harbin, China, 24–26 December 2011; Volume 2, pp. 1181–1185. [[CrossRef](#)]
18. Tian, Y.; Mai, Z.; Zeng, Z.; Cai, Y.; Yang, J.; Zhao, B.; Zhu, X.; Qi, L. Design and experiment of an integrated navigation system for a paddy field scouting robot. *Comput. Electron. Agric.* **2023**, *214*, 108336. [[CrossRef](#)]
19. Li, S.; Zhang, M.; Ji, Y.; Zhang, Z.; Cao, R.; Chen, B.; Li, H.; Yin, Y. Agricultural machinery GNSS/IMU-integrated navigation based on fuzzy adaptive finite impulse response Kalman filtering algorithm. *Comput. Electron. Agric.* **2021**, *191*, 106524. [[CrossRef](#)]
20. Ren, H.; Wu, J.; Lin, T.; Yao, Y.; Liu, C. Research on an Intelligent Agricultural Machinery Unmanned Driving System. *Agriculture* **2023**, *13*, 1907. [[CrossRef](#)]

21. Zhang, L.; Zhu, X.; Huang, J.; Huang, J.; Xie, J.; Xiao, X.; Yin, G.; Wang, X.; Li, M.; Fang, K. BDS/IMU Integrated Auto-Navigation System of Orchard Spraying Robot. *Appl. Sci.* **2022**, *12*, 8173. [[CrossRef](#)]
22. Inoue, K.; Kaizu, Y.; Igarashi, S.; Imou, K. The development of autonomous navigation and obstacle avoidance for a robotic mower using machine vision technique. *IFAC-Pap.* **2019**, *52*, 173–177. [[CrossRef](#)]
23. Yang, Q.; Qu, D.; Xu, F.; Zou, F.; He, G.; Sun, M. Mobile robot motion control and autonomous navigation in GPS-denied outdoor environments using 3D laser scanning. *Assem. Autom.* **2019**, *39*, 469–478. [[CrossRef](#)]
24. Zhang, Q.; Chen, M.S.; Li, B. A visual navigation algorithm for paddy field weeding robot based on image understanding. *Comput. Electron. Agric.* **2017**, *143*, 66–78. [[CrossRef](#)]
25. Zhang, S.; Guo, C.; Gao, Z.; Sugirbay, A.; Chen, J.; Chen, Y. Research on 2D Laser Automatic Navigation Control for Standardized Orchard. *Appl. Sci.* **2020**, *10*, 2763. [[CrossRef](#)]
26. Sharma, S.; Deka, K.; Mandloi, M. Deep Learning Noncoherent UWB Receiver Design. *IEEE Sens. Lett.* **2021**, *5*, 1–4. [[CrossRef](#)]
27. Zhou, N.; Lau, L.; Bai, R.; Moore, T. Novel prior position determination approaches in particle filter for ultra wideband (UWB)-based indoor positioning. *Navigation* **2021**, *68*, 277–292. [[CrossRef](#)]
28. Pastell, M.; Frondelius, L.; Järvinen, M.; Backman, J. Filtering methods to improve the accuracy of indoor positioning data for dairy cows. *Biosyst. Eng.* **2018**, *169*, 22–31. [[CrossRef](#)]
29. Hindermann, P.; Nüesch, S.; Früh, D.; Rüst, A.; Gygax, L. High precision real-time location estimates in a real-life barn environment using a commercial ultra wideband chip. *Comput. Electron. Agric.* **2020**, *170*, 105250. [[CrossRef](#)]
30. Xie, B.; Liu, J.; Cai, L.; Xu, Z.; Hou, G.; Wang, J.; Li, Y. Design of the UWB navigation system for tracked agricultural machinery in small land and analysis of base station layout. *Trans. CSAE* **2022**, *38*, 48–58. [[CrossRef](#)]
31. Yao, L.; Hu, D.; Zhao, C.; Yang, Z.; Zhang, Z. Wireless positioning and path tracking for a mobile platform in greenhouse. *Int. J. Agric. Biol. Eng.* **2021**, *14*, 216–223. [[CrossRef](#)]
32. Yao, L.; Pitla, S.K.; Yang, Z.; Xia, P.; Zhao, C. Path tracking of mobile platform in agricultural facilities based on ultra wideband wireless positioning. *Trans. CSAE* **2019**, *35*, 17–24.
33. Yuan, X.; Bi, Y.; Hao, M.; Ji, Q.; Liu, Z.; Bao, J. Research on Location Estimation for Coal Tunnel Vehicle Based on Ultra-Wide Band Equipment. *Energies* **2022**, *15*, 8524. [[CrossRef](#)]
34. Liu, Y. UWB ranging error analysis based on TOA mode. *J. Phys. Conf. Ser.* **2021**, *1939*, 012124. [[CrossRef](#)]
35. Liu, A.; Lin, S.; Wang, J.; Kong, X. A Novel Loosely Coupling Fusion Approach of Ultra-Wideband and Wheel Odometry for Indoor Localisation. *Electronics* **2023**, *12*, 4499. [[CrossRef](#)]
36. Zou, A.; Hu, W.; Luo, Y.; Jiang, P. An Improved UWB/IMU Tightly Coupled Positioning Algorithm Study. *Sensors* **2023**, *23*, 5918. [[CrossRef](#)] [[PubMed](#)]
37. Jiang, P.; Hu, C.; Wang, T.; Lv, K.; Guo, T.; Jiang, J.; Hu, W. Research on a Visual/Ultra-Wideband Tightly Coupled Fusion Localization Algorithm. *Sensors* **2024**, *24*, 1710. [[CrossRef](#)]
38. Li, L.; He, X.; Xiao, Y.; Jiao, T.; Li, W. Design and Experimental Verification of Targeted and Variable Sprayer for the Potato. *Agriculture* **2023**, *13*, 797. [[CrossRef](#)]

**Disclaimer/Publisher’s Note:** The statements, opinions and data contained in all publications are solely those of the individual author(s) and contributor(s) and not of MDPI and/or the editor(s). MDPI and/or the editor(s) disclaim responsibility for any injury to people or property resulting from any ideas, methods, instructions or products referred to in the content.